In-flame and in-cylinder flow/turbulence measurements near the glow plug using flame image velocimetry and particle image velocimetry in an optical compression-ignition engine

J. Yang[1], S. Kook[1,*], K. Kim[2], C. Kweon[2]
1: The University of New South Wales, Sydney, Australia
2: DEVCOM Army Research Laboratory, Aberdeen Proving Ground, MD, USA
* Correspondent author: s.kook@unsw.edu.au

Keywords: PIV, FIV, glow plug, flow fields, turbulence intensity

ABSTRACT

The present study implements two diagnostic methods based on tracking of seeded olive oil droplets (PIV: particle image velocimetry) and pattern changes detected in high-speed flame movies (FIV: flame image velocimetry) in a small-bore optical diesel engine. For each measurement, a total of 100 engine cycles are recorded and processed to address the inherent cyclic variations. The ensemble-averaged flow fields and turbulence intensity distribution extracted from individual cycles via the spatial filtering method are discussed with a particular interest in the influence of glow plug on flow and turbulence, *i.e.* rigid body and fluid interaction. The PIV results show a swirl flow structure forms and rotates with its centre shifted towards the exhaust side, leading to an asymmetric swirl structure. By comparing a PIV laser plane tilted towards the glow plug and a 10 mm horizontal plane below the cylinder head with no glow flow-plug interaction, it is observed that the flow-plug interaction causes the flow winding around the plug tip to generate complex flow structures and new vortices downstream of the plug. The tilted plane and 10-mm plane show similar bulk flow magnitude distribution patterns; however, the flow-plug interaction generates high turbulence in the tilted plane right downstream of the plug tip where new vortices form, which lasts for a few crank angles. The spatially averaged flow magnitude and turbulence intensity are measured higher in the 10-mm plane where there is no flow-plug interaction, suggesting the increased turbulence is a localised behaviour. The flame-plug interaction is also investigated during the combustion event using the FIV method. The level of flame-plug interaction is adjusted by changing the inter-jet spacing angle of two nozzle holes with one case showing high interaction and the other displaying low interaction. From the FIV measurements, the most significant effect of the flame-plug interaction is observed as the further penetration of the wall bounced flame for the high interaction case. This is due to the glow plug as a rigid body blocking the swirl flow and promoting the flame penetration back towards the centre of the combustion chamber upon the piston-bowl wall impingement. The measured turbulence intensity is also higher thanks to the enhanced wall bounced flame in addition to more significant flame-plug interaction at the interface.

1. Introduction

While diesel engines are favoured for their high thermal efficiency and reliability, the emission issues (*e.g.* particulate matter and NOx) raise the concern due to the adverse impacts on the environment and human health (Broday & Rosenzweig, 2011; Jacobson, 2010). The in-cylinder flow development in a diesel engine significantly affects the air-fuel mixing process, and in turn engine-out emissions. In a typical diesel engine, a swirl flow is generated as the air is induced into the cylinder through a spiral-shaped flow passage (Payri et al., 2004; Rabault et al., 2016). The swirl flow represented the mean bulk flow motion, which survives during the compression and exhaust stroke (le Roy & le Penven, 1998). Therefore, the swirl flow in diesel engines makes a significant impact on the mixing and combustion.

When the diesel fuel is directly injected into the cylinder, the injection induced flow alters the existing flow motion and leads to a more complex flow structure. Upon the fuel injection, the diesel fuel jets impinge on the piston-bowl wall and subsequently interact with the in-cylinder swirl flow to cause jet-wall interaction (Genzale et al., 2009) and jet-swirl interaction (Zhang et al., 2019). Given these flow phenomena directly impact the mixing and combustion, there is a great demand for the flow and turbulence measurements in a running engine.

To the measurement of complex flow structures in an engine environment, the two-dimensional, time-resolved flow field imaging based on Particle Image Velocimetry (PIV) is widely used (Cosadia et al., 2007; Miles et al., 2007; Reuss et al., 1995; Zeng et al., 2015). High-speed imaging is performed using seeding particles mixed with the intake air, which are illuminated with the incident of laser light. The particle movements are tracked, which are used to extract flow vectors based on a cross-correlation algorithm applied to the frame pairs with very short temporal separation (Westerweel, 1997). The PIV applications have achieved many findings in diesel engines including in-cylinder flow structure visualisation (Heim & Ghandhi, 2011; Neal et al., 2013; Zeng et al., 2014), swirl ratio calculation and validation of numerical modelling of in-cylinder flow (Baum et al., 2014). However, due to the strong interference from laser scattering on seed particles and broadband soot luminosity, PIV measurement is limited to non-reacting conditions (Malbec & Bruneaux, 2010). To overcome this hurdle, a PIV algorithm is applied to high-speed soot luminosity photographs (H. W. R. Dembinski, 2014; Shioji et al., 1989) to use variations in image contrast caused by in-flame pattern change as a tracking source. This is termed "Flame Image Velocimetry (FIV)" or "Combustion Image Velocimetry (CIV)" with its successful application found in many diesel engine studies (H. Dembinski et al., 2013; H. Dembinski & Angstrom, 2013a, 2013b; H. W. R. Dembinski & Angstrom, 2012; Winterbone et al., 1994; Zha et al., 2018; Zhao & Kaiser, 2018).

The present study applies both PIV and FIV in a small-bore optical diesel engine with a particular interest in the effect of glow plug as a rigid body and its interaction with the swirl flow and the flame. With enhanced knowledge on the swirl-plug interaction and flame-swirl interaction, hidden potentials of diesel engine efficiency improvement and further emissions reduction could be found.

2. Experiment

2.1 Optical diesel engine

The experiments were conducted in a single-cylinder, small-bore optical diesel engine, as shown in Figure 1. This optical diesel engine was modified from a conventional four-cylinder 1.6-litre engine with three cylinders deactivated. The engine specifications and operating conditions are summarised in Table 1. The active cylinder has 77.2 mm bore and 84.5 mm stroke, resulting in a displacement volume of 395.5 cm^3. The compression ratio is 16.2 which is typical for modern light-

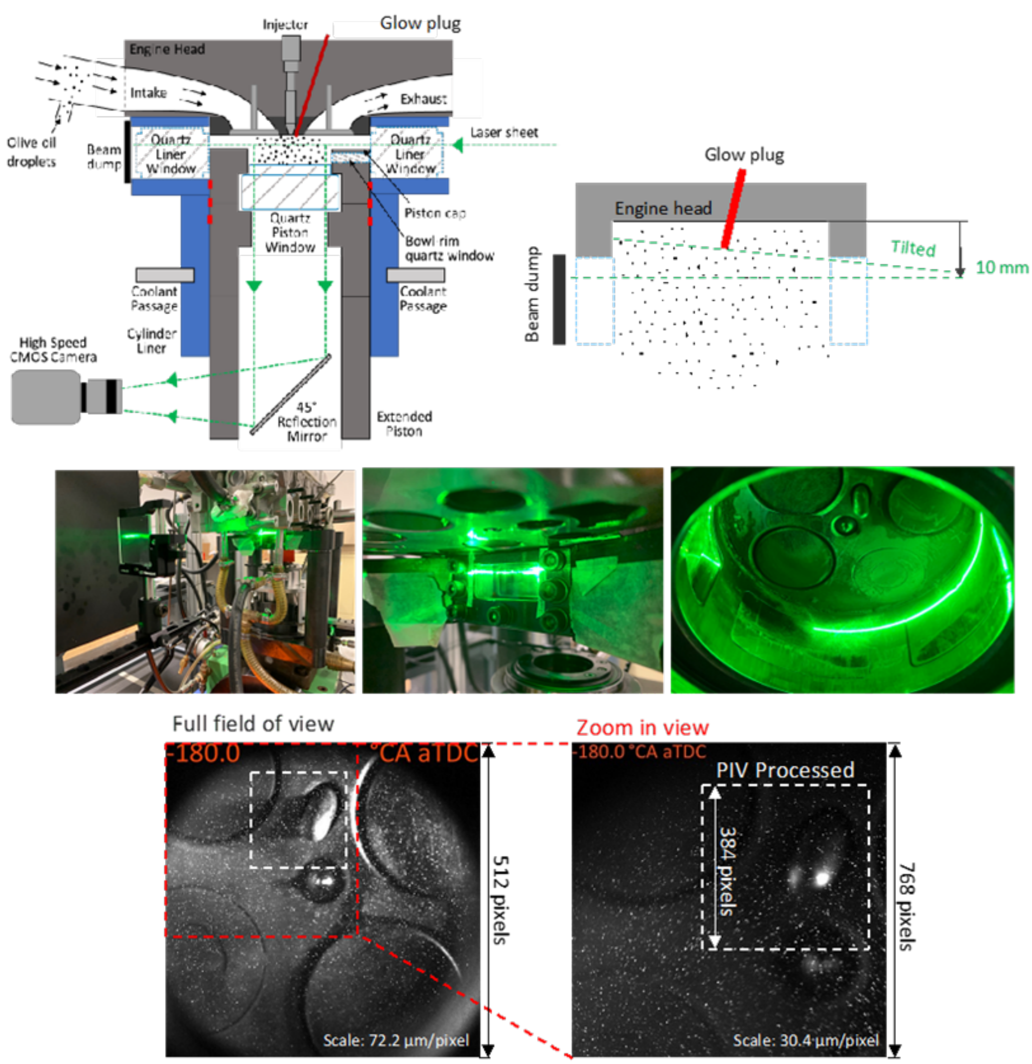

Fig. 1 Optical diesel engine and PIV diagnostic setup (top), setup photos (middle) and two selected PIV field of views (bottom).

duty diesel engines. This engine has a swirl ratio of 1.7 when no port throttling is used. Figure 1 shows the simplified illustration of the optical engine. The optical access was achieved via the quartz window installed on the extended piston top together with a 45° reflection mirror in the bottom-view orientation. Four liner quartz windows also allow for the optical access that are used for the laser beam insertion in PIV experiments.

The engine was operated at fixed speed of 1200 rpm using an AC electric motor, which was connected directly to the flywheel/crankshaft. The intake air temperature was measured at 303 K (*i.e.* room temperature), which was held constant throughout the experiment. To simulate a warmed up and thermally stable engine condition, the temperature of coolant flowing through the cylinder head, liner and engine block was maintained at 363 K. This was done using a water heater/circulator (Thermalcare Aquatherm RQE0920). A common rail system (Bosch CR/V4/10-12 S) was utilised for the direct injection of conventional ultra-low sulphur diesel (cetane number of 51) using a top-mounted solenoid injector (Bosch CR12-20). The injectors used for the FIV measurement had a two-hole-nozzle configuration with each hole having a nominal hole diameter of 120 μm. The nozzle was modified from a conventional 8-hole injector by laser-welding unused 6 holes.

The optical engine was operated at 10 skip-firing mode as the fuel injection occurs every 9 motoring cycles, *i.e.* 9 no-injection cycles followed by one injection cycle. The skip firing operation was useful to maintain low thermal loading on quartz windows and to expel residual gases from the previous firing cycle for lower cyclic variations. The in-cylinder pressure was measured using a piezoelectric pressure transducer (Kistler 6056A) installed on the engine head at a sampling frequency of 100 kHz (corresponding to 0.072 °CA resolution at 1200 rpm). The data of in-cylinder pressure was recorded and processed through in-house developed Matlab code, using a charge amplifier (Kistler 5015) and a data acquisition device (MCC USB-1616HS-BNC).

2.2 PIV and FIV diagnostic setup

For high-speed PIV measurements, an Nd:YLF PIV laser (Litron LDY303HE) was used in the present study, which has an output at 527 nm wavelength. As listed in Table 2, the laser was operated at a double-pulse mode with pulse separation of 20 μs. The pulse repetition rate was set at 10 kHz, leading to 0.72 °CA at 1200 rpm separation between the PIV-derived flow vectors. The horizontal laser sheet in the swirl plane was produced using a set of plano lenses similar with the previous study (Clark & Kook, 2018). It was inserted through the cylinder liner window (and through the bowl-rim window near top dead centre) at 10 mm below the cylinder head. This setup was to obtain flow vectors in the r-θ swirl plane. For the measurement of the flow directly

Table 1 Engine specification and operating conditions.

Displacement	395.5 cm^3
Bore size	77.2 mm
Stroke length	84.5 mm
Compression ratio	16.2
Swirl ratio	1.7 (base) and higher swirl
Engine speed	1200 rpm (higher speed in consideration)
Intake temperature	303 K
Wall (coolant) temperature	363 K
Fuel	Conventional diesel and CN30
Injection system	Solenoid Injector (Bosch CR12-20) Common rail (Bosch CR/V4/10-12S)
Number of holes	2 (6 laser welded from 8 original holes)
Rail pressure	70 MPa
Injection timing (electronic)	11 and 13°CA bTDC
Inter-jet angle	45° and 90°

Table 2 PIV measurement conditions.

Imaging rate	10 kHz
Pulse separation	20 μs
Resolution	512 × 512 pixels (72.2 μm/pixel) 768 × 768 pixels (30.4 μm/pixel)
Laser plane height	Tilted plane 6 mm and horizontal plane 10 mm below cylinder head

interacting with the glow plug as a rigid body, the laser beam was tilted up as illustrated in Figure 1. The frame rate of the high-speed camera was set at 10 kHz with a double-frame mode. The trigger of imaging was synced with the start of fuel injection, and the laser pulse-camera sync was controlled using a timing unit (LaVision PTU X). The image resolution was 512 by 512 pixels for the full field of view imaging. For the higher resolution measurement around the glow plug, 768 by 768 pixel image was taken. The high speed imaging was done via a high-speed CMOS camera (Photron FASTCAM SA-X2) with a 200-mm focal length Nikkor lens at the aperture of f/8. For PIV seeding, olive oil was selected primarily because it flows with the air easily and returns very high signal quality (Clark & Kook, 2018). Solid particles were also considered (*e.g.* widely used SiO2) but, given the main use of PIV in this study is for in-cylinder swirl flow measurements prior to the fuel injection, olive oil was preferred. An olive oil atomiser was used to generate the oil droplets with nominal diameter of 1 μm. The droplets were supplied into the engine at around 300 mm upstream of the intake port to ensure homogeneous dispersion in the intake air. The seeding rate was controlled by adjusting the inlet air pressure of the oil atomiser for the best signal quality.

Table 3 Camera settings for the FIV measurement.

Imaging rate	45 kHz
Pulse separation	22.2 μs (0.16 °CA)
Resolution	512 × 512 pixels (72.2 μm/pixel)

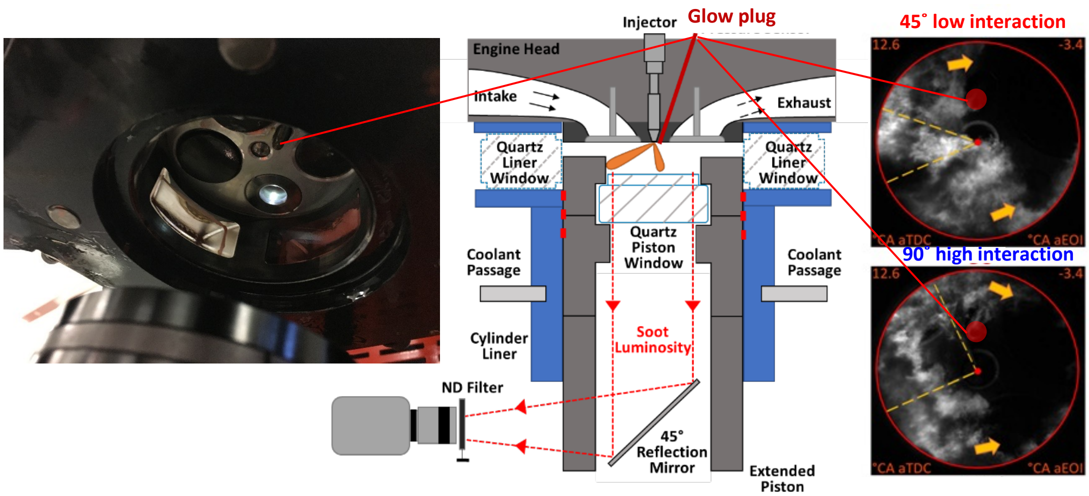

Fig. 2 Optical engine and camera setup for high-speed soot luminosity imaging.

Figure 2 shows the high-speed flame imaging setup. The same camera and lens were used as the PIV measurement, yet the aperture was set to f/32 and the exposure time was minimised to 1 μs to accommodate the high intensity of the broadband soot luminosity signals in the case of FIV measurement. In addition, neutral-density (ND) filters were placed in front of the camera lens to avoid signal saturation which may lead to the failure of vector derivation and to achieve the best signal contrast for FIV analysis. As summarised in Table 3, the camera allows for a maximum frame rate of 45 kHz at image resolution of 512 by 512 pixels, which results in a fine-scale of 72.2 μm/pixel suitable for flow decomposition into a low-frequency bulk flow component and a high-frequency fluctuating component (Adrian et al., 2011; Yang et al., 2020). A total of 100 individual firing cycles were executed and recorded at each test condition, which was used for ensemble averaging of measured flow fields. Figure 2 shows two nozzle holes used for the study of flame-glow plug interaction. The nozzle with 45° inter-jet spacing angle has holes distant from the glow plug and thus the flame-plug interaction is low. On the other hand, the 90° inter-jet spacing nozzle has one fuel jet directly interacting with the glow plug and thus is marked as a high interaction case.

2.3 PIV/FIV data processing

The PIV and FIV used in this study share the same principle in obtaining flow vectors from trackable signals of the object with it being laser illuminated oil droplets (PIV) or small-scale flame patterns (FIV). Therefore, for both FIV and PIV, the obtained high-speed movies were post processed using a PIV software (Lavision DaVis 10.0.4). To increase the accuracy of derived velocity vectors, all processing parameters were optimised through parameter by parameter evaluation.

Figure 3 shows an overview of the PIV data processing of the present study. For velocity vector derivation, a multi-pass Fast Fourier Transform (FFT) cross-correlation algorithm was performed on every consecutive frame pair, in which the laser-illuminated droplet displacement was tracked. In this process, the cross-correlation coefficients were computed through pixel-wise comparison performed within interrogation windows, *i.e.* sub-regions of the original image. The velocity vector was calculated from the most probable displacement, which was determined through a Gaussian 3-point estimator finding the peak value in correlation matrix. According to the quarter rule (Adrian et al., 2011), the interrogation window size should be larger than 4 times of the largest particle displacement. In this regard, 16-pixel final window size was selected for higher resolution. A 12-pass interrogation window setting was implemented, starting from a 96-pixel window to a final window size of 16 pixels. Through iterations, the calculated vectors were refined in each pass at a 50% overlap with the final vector resolution of 8 pixels. In addition, spurious vectors were

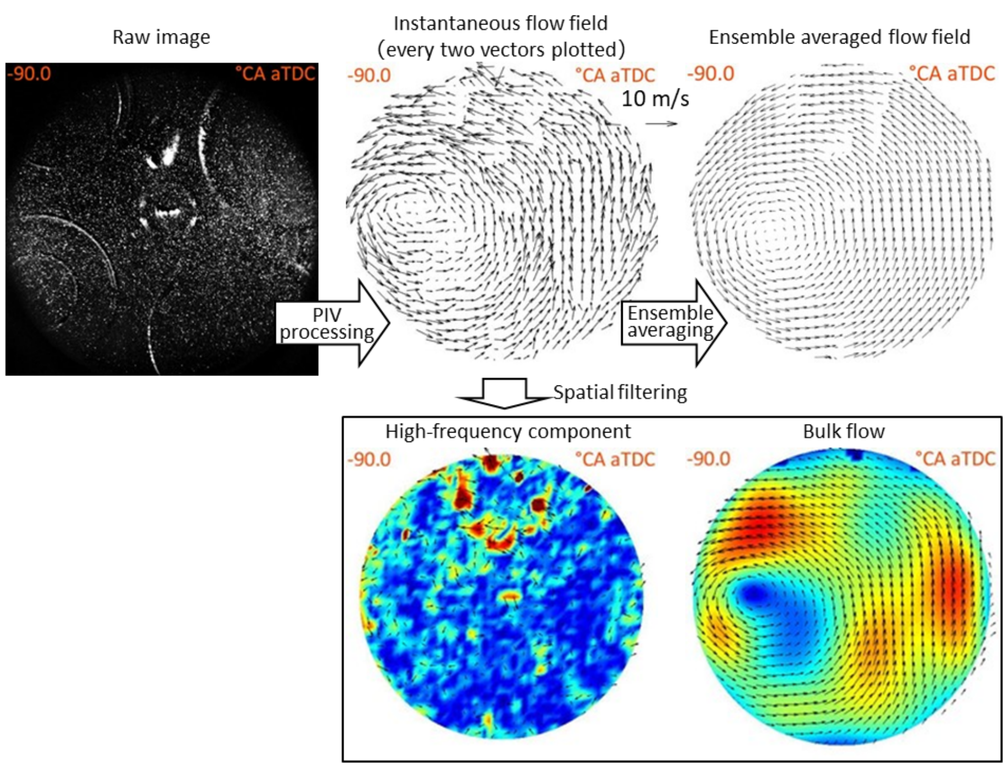

Fig. 3 PIV processing procedures.

identified using the universal outlier detection. These vectors were removed and replaced using a median filter in each localised region. The threshold of this median filter was set at 2 with a filter region of 3 × 3 vectors, consistent with a previous study (Westerweel & Scarano, 2005). The resulting instantaneous flow vectors are shown on the top-middle of Figure 3. However, the original pixel resolution was too high to observe the flow structure details due to very dense vectors. For the presentation purpose, the flow fields were plotted with only half the original vectors. The processing was repeated for 100 motored engine cycles and the ensemble-averaged flow field was obtained as shown on the top-right corner of Figure 3.

For the FIV processing, contrast variations in soot luminosity signals due to flame pattern evolution were tracked to derive flow fields. Figure 4 shows an example of FIV data processing. The raw flame image on the left of Figure 4 was pre-processed using a 3×3 Gaussian smoothing filter to reduce the background noise. This was followed by a sharpening filter for contrast enhancement. The cross-correlation algorithm as in the PIV processing was applied to the pre-processed images to derive the flow fields within the flame (*i.e.* in-flame flow vectors). The universal outlier detection was used to remove erroneous vectors, and the instantaneous vector field was obtained as displayed at the top-middle of Figure 4. The process was repeated for 100 fired cycles to obtain the ensemble averaged flow field as shown on the top-right corner of Figure 4.

It may be argued that the off-plane flow motion outside the r-θ plane (*i.e.* horizontal plane) would impact the obtained flow vectors. The line-of-sight integrated nature of the soot luminosity signals for FIV measurement leads to the derived flow fields representing the spatially averaged flow field development with the off-plane motions included. However, the flame structure development is

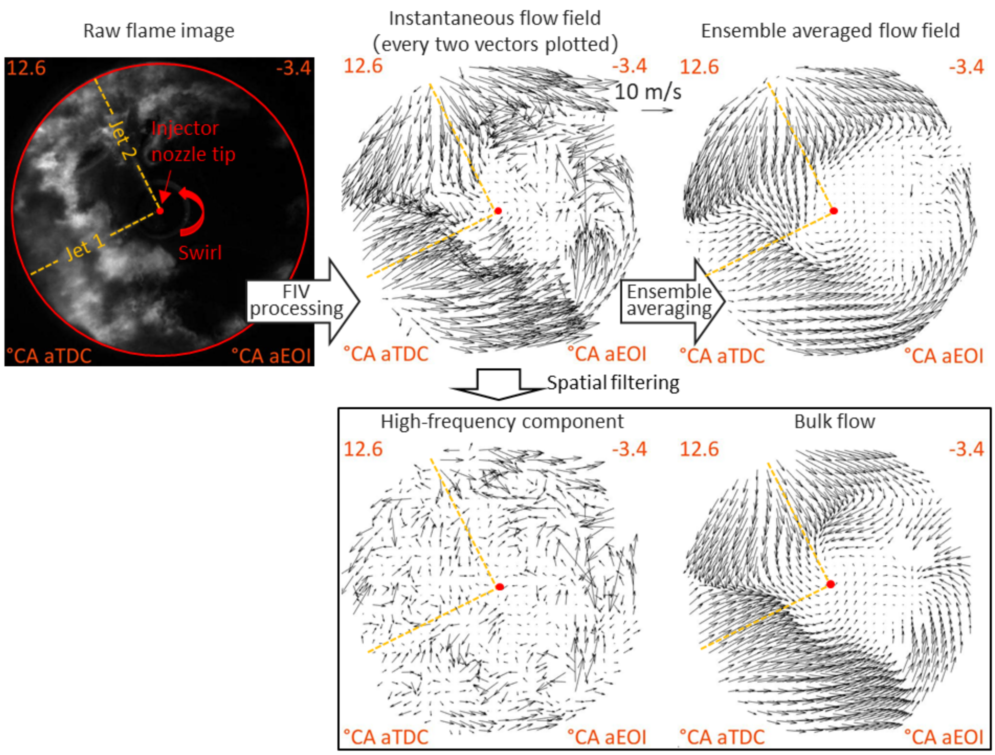

Fig. 4 FIV processing procedures.

predominantly driven by the r-θ flow motion during the main combustion period. Hence, the effect of flame movements in other direction (*e.g.* the r-z vertical plane) is deemed insignificant. Also, it was noted the in-flame flow measurements would not be possible using the PIV due to strong signal interference from the broadband soot signals as shown in Figure 4. Using solid seed particles, the PIV might return flow vectors outside the flame area; however, the diesel flames dominate the entire combustion chamber and thus the flow field measurement during the combustion event is not possible. The FIV of the present study, despite its own limitations, can provide these in-flame flow vectors.

2.4 PIV/FIV flow decomposition

To the flow vectors obtained from the PIV and FIV processing, the Reynolds decomposition was implemented to separate the bulk flow from fluctuating flow using the in-house developed Matlab code. The bulk flow component represents the low-frequency mean flow field whereas the high-frequency fluctuating component includes flow turbulence. Given the obtained vectors contain time-resolved, two-dimensional information, the spatial filtering approach was used for each imaging timing. The Reynolds decomposition was performed using the following equations:

$$U(t,x,y,i) = \overline{U}_{EA}(t,x,y) + u'(t,x,y,i) \quad (1)$$

$$\overline{U}_{EA}(t,x,y) = \frac{1}{N}\sum_{i=1}^{N} U(t,x,y,i) \quad (2)$$

where $U(t,x,y,i)$ is the instantaneous velocity, $u'(t,x,y,i)$ is the fluctuation velocity at crank angle timing t and at location (x, y) in cycle i. The $\overline{U}_{EA}(t,x,y)$ is the ensemble average over 100 cycles. The calculated fluctuation of instantaneous cycle flow vectors is primarily due to cyclic variations rather than turbulence during engine operations (Clark & Kook, 2018). To obtain high-frequency fluctuations caused primarily by flow turbulence, a spatial filtering method was applied to each individual cycle, which was performed as:

$$U(t,x,y,i) = U_{bulk}(t,x,y,i) + u'_{hf}(t,x,y,i) \quad (3)$$

where $U_{bulk}(t,x,y,i)$ is the low-frequency flow (*i.e.* bulk flow) velocity according to a low-pass filter and $u'_{hf}(t,x,y,i)$ is the high-frequency fluctuating velocity at crank angle timing t at location (x, y) in cycle i. Example bulk flow field and high-frequency fluctuating components obtained from this spatial filtering method are shown in Figure 3 and 4 (bottom). It is noted that the selection of low-pass filter size in this spatial filtering approach remains arbitrary for in-cylinder flows. In the present study, the filter size was optimised until the filtered low-frequency component ($U_{bulk}(t,x,y,i)$) resembles the ensemble averaged flow field ($\overline{U}_{EA}(t,x,y)$) the most. It was noted lower cut-off length led to over-estimation of large-scale vortices in the bulk flow whereas the higher cut-off length caused over-simplified bulk flow.

3. Results and Discussion

3.1 PIV derived flow fields

Figure 5 shows the ensemble averaged flow fields of 100 individual cycles for seven selected crank angles during the intake and compression strokes. The development of in-cylinder flow fields is clearly seen from these PIV derived flow vectors. During the intake stroke, strong and chaotic flow vectors are noticed as the flow components from two intake valves merge and interact with the piston bowl wall. The flow is particularly complex at the top-left corner of the cylinder where the air is induced into the cylinder towards the exhaust valve side, *i.e.* downstream of the intake flow and the plug, which is more pronounced for the tilted plane due to high interaction with the plug. For example, at -285.1 °CA aTDC, the flow vectors winding around the plug tip are clearly shown in the tilted plane which are not observed in the 10 mm plane, indicating the noticeable influence

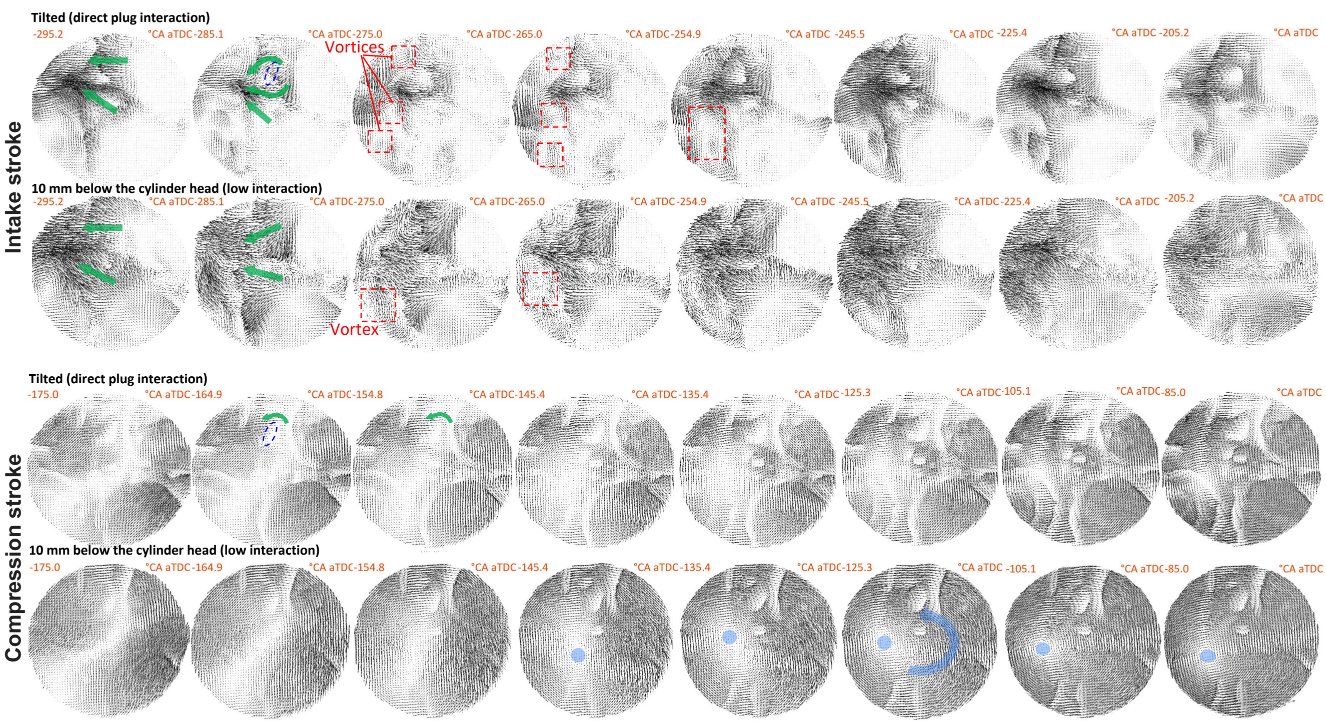

Fig. 5 100 cycle averaged PIV flow fields of tilted plane and 10 mm plane during the intake stroke and compression stroke.

of the plug tip as a rigid body on the intake flow. This additional flow component formed due to the flow-plug interaction leads to enhanced vortex formation on the left side, as shown by the red dashed boxes from -275 °CA aTDC to -254.9 °CA aTDC. More vortices are generated in the titled plane and distributed in larger area downstream of the intake flow and plug, as compared to the 10 mm plane. In later crank angles, the swirling flow structure initiates for both planes. Regarding the compression stroke, the flow vectors gradually settle down and swirl flow structure becomes more evident which is not significantly influenced by the plug presence. The flow vectors developing around the plug tip can still be observed which are however not clear as that during the intake period. Given the 10 mm plane is a horizontal flow in r- θ plane, the well-defined swirl flow structure in the counter-clockwise direction appears earlier (*e.g.* -154.8 °CA aTDC) and more clearly, comparing to the flow in the titled plane. The swirl centre identified from visual inspection is found on the left side and gradually shifts following the path in the same direction of swirl flow. The resulting asymmetric swirl structure due to the spiral passage shape of the lower intake port is consistent with a previous study (Zha et al., 2015).

Figure 6 shows the 100-cycle averaged zoom-in PIV flow fields around the glow plug for the tilted and 10 mm plane during the intake stroke and compression stroke. For plug tip focused flow analysis with much higher spatial resolution, the flow fields were processed in the zoom-in region near the plug tip, in which the image resolution was also increased from 512 by 512 pixels to 768 by 768 pixels. During the intake stroke, the flow winding around the plug tip is clearly shown by the flow vectors in the tilted plane, as in the full field view in Figure 5. The vortex structures resulting from flow-plug interaction are again observed in these zoom-in flow fields. Two vortices form near the plug and gradually merge between -285.1 and -265 CA °aTDC. After the strong intake flow period, the flow field is stabilised, and the plug tip appears as a stagnation area at -205.2 °CA aTDC. The flow vectors in the 10 mm plane are more chaotic during the intake as the

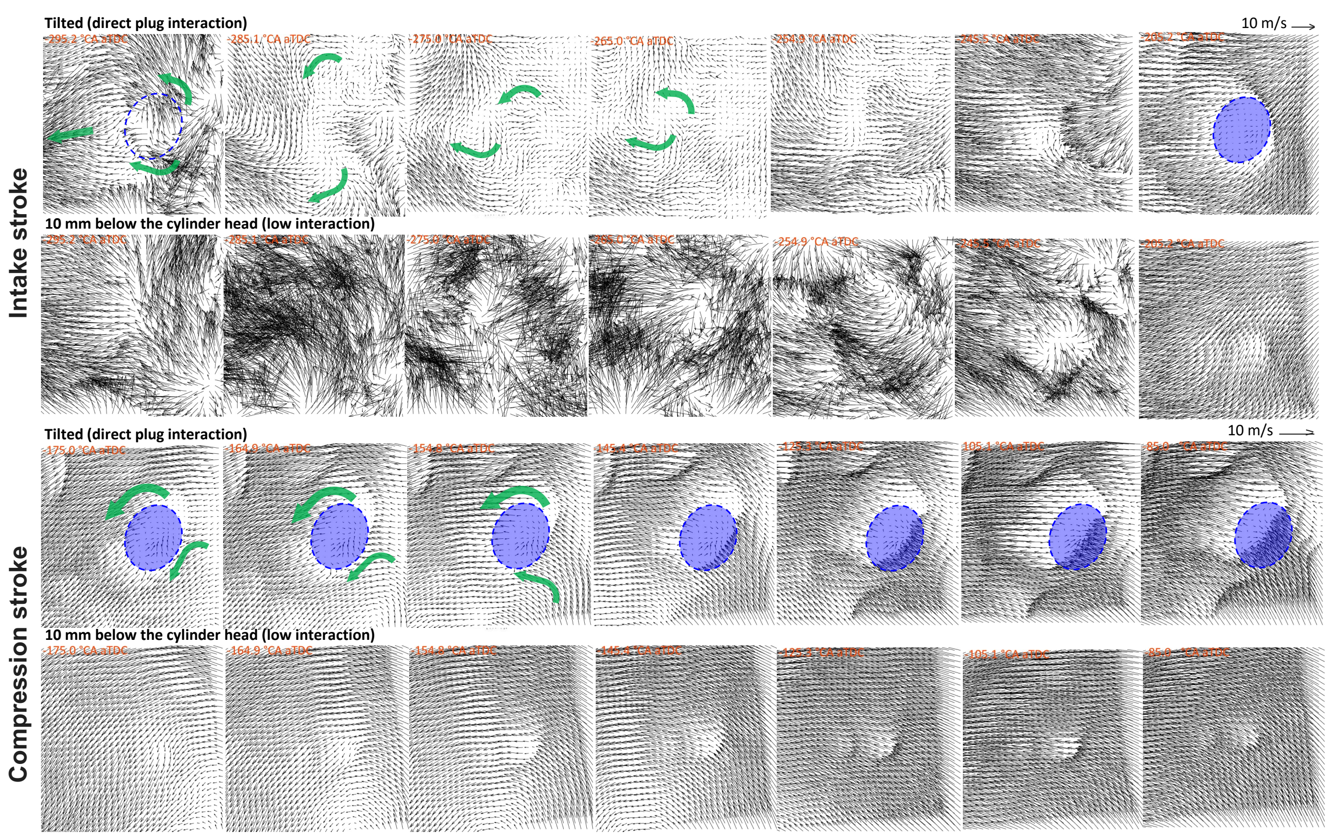

Fig. 6 100-cycle averaged PIV flow fields zoomed in around the glow plug for the tilted and 10 mm plane during the intake stroke and compression stroke.

piston moves down to the bottom dead centre (BDC). The flow vectors become clearer in later crank angles after -205.2 °CA aTDC, showing a single flow component in the counter-clockwise direction. For the compression stroke, the flow vectors become almost unidirectional due to the swirl formation. The tilted plane, due to the direct flow-plug interaction, shows the flow vectors winding around the plug tip region while the swirl flow structure is not significantly altered. The 10 mm plane only displays the swirl flow structure in the counter-clockwise direction.

3.2 Bulk flow magnitude and turbulence intensity during intake and compression strokes

To the analysis of distribution of bulk flow magnitude and turbulence intensity, the corresponding contour plots are shown in Figure 7 and Figure 8, respectively. As discussed previously, the flow-plug interaction during intake stroke leads to additional flow component around the plug tip, which is also shown in the bulk flow contour plots in Figure 7. The tilted plane exhibits a very

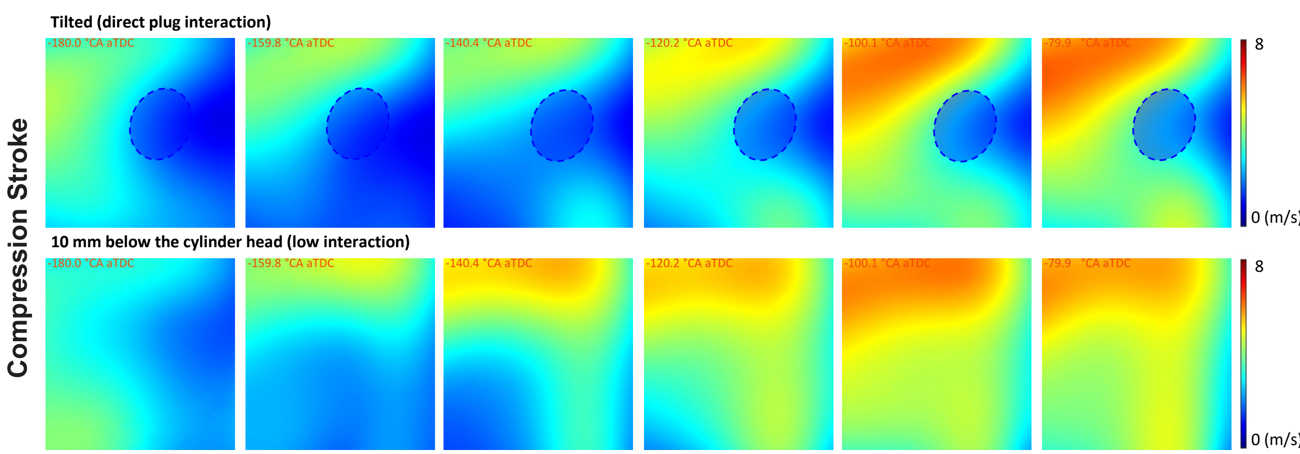

Fig. 7 100-cycle averaged PIV bulk flow vector magnitude distribution of tilted plane and 10 mm plane during the compression stroke.

high flow magnitude region on the top-left corner. This is the downstream region of the flow

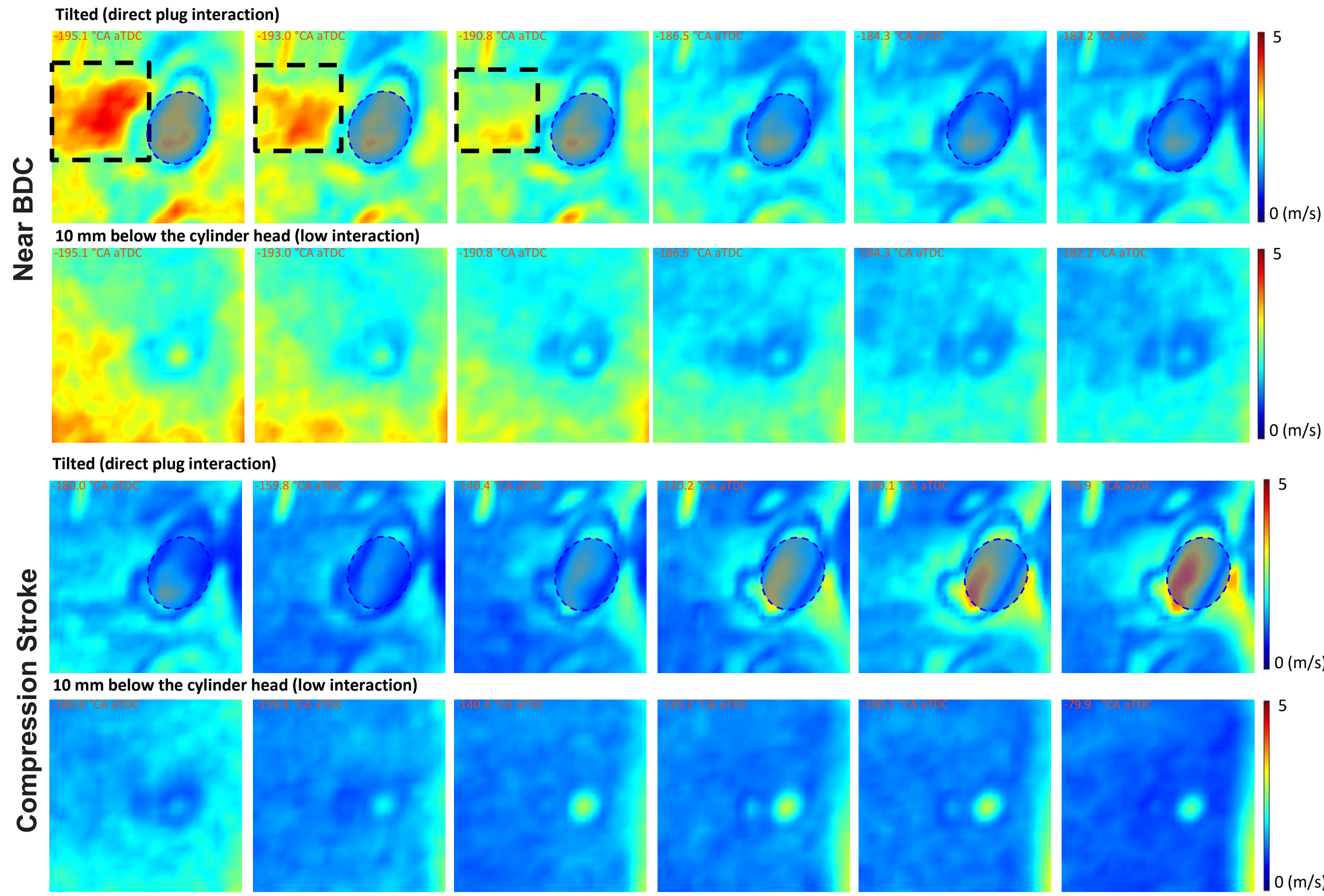

Fig. 8 100-cycle averaged PIV turbulence intensity distribution of tilted plane and 10 mm plane near BDC timings and during the compression stroke.

winding around the plug tip. The magnitude become uniform for the swirl flow structure in the 10 mm planes. Regarding the turbulence intensity, noticeable differences are shown in the contour plots in Figure 8. High turbulence region (highlighted by the black dashed boxes) due to the flow-plug interaction is found when the swirl flow formation occurs at around bottom dead centre (BDC). The tilted plane shows high turbulence intensity right downstream of the plug tip, which lasts for a few crank angles. This is a result of new vortex formation, which was produced due to the flow vectors winding around the plug tip, indicating the flow-plug interaction induced turbulence. The 10 mm plane shows high turbulence at -195~-193 °CA aTDC due to remaining high intake flow. However, there is no high turbulence region as in the tilted plane due to the lack of flow-plug interaction.

3.3 Raw flame images and FIV derived flow fields

To the flow analysis with the influence of plug during combustion, FIV was applied to obtain the in-flame flow fields. Figure 9 shows the ensemble averaged in-cylinder pressure traces of high and

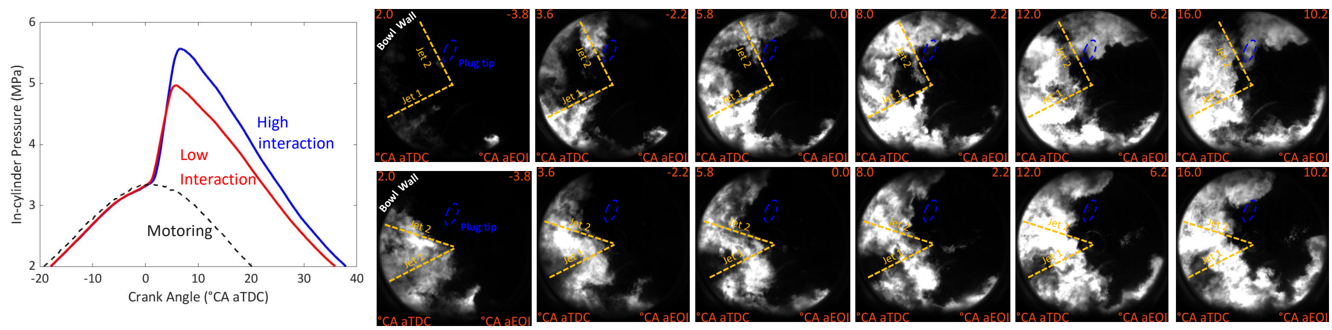

Fig. 9 In-cylinder pressure of motored and fired engine cycles (left) and selected flame images of high flame-plug interaction (90° inter-jet spacing two-hole nozzle, top row) and low flame-plug interaction (45° inter-jet spacing two-hole nozzle, bottom row).

low flame-plug interaction conditions (90° and 45° inter-jet spacing two-hole nozzle, respectively). The corresponding flame images at six selected crank angles are presented on the right. The pressure traces show that higher peak in-cylinder pressure is measured for the high interaction condition due to better mixing from reduced jet-jet interaction of 90° inter-jet spacing. The flame images show that the flames initially develop along the jet axes, travelling along the bowl wall and bouncing back towards the nozzle. The jet-to-jet interaction is noticed, which is more significant for the smaller spacing angle nozzle. It is noted that, the jet 2 flame for 90° inter-jet spacing develops in the vicinity of the plug, and then the wall bounced flame penetration is influenced by the plug. In comparison, there is no direct flame-plug interaction for 45° nozzle which only shows late cycle flame flowing around the ignition assistance plug tip. Therefore, a region of interest for detailed FIV analysis is selected near jet 2 for the high and low flame-plug interaction cases. It is noted the glow plug was not operated and thus only acted as a rigid body, consistent with PIV results in the previous sections.

Figure 10 shows the 100-cycle averaged FIV derived flow fields of the high and low flame-plug interaction cases in the 60° sector region for the right side of Jet 2 axis. The glow plug is illustrated for the high interaction case whereas the glow plug is outside the region of interest for the low interaction condition. Clear flame-wall interactions on the up-swirl side of jet 2 are shown by the flow vectors which develop along the wall and bounce back towards the nozzle. The initial development of vectors shows no significant effect of the plug tip during fuel injection due to high jet momentum for both high and low interaction cases. However, upon the end of injection, the wall bounced flame penetrates further towards the nozzle without being laterally shifted by the swirl flow for the high interaction case. In comparison, with an emphasis on the corresponding plug tip region of the high interaction nozzle, the low interaction case displays flow vectors quickly swept away by the swirl flow. This suggests the plug tip blocked the swirl flow so that the wall bounced flame could penetrate further.

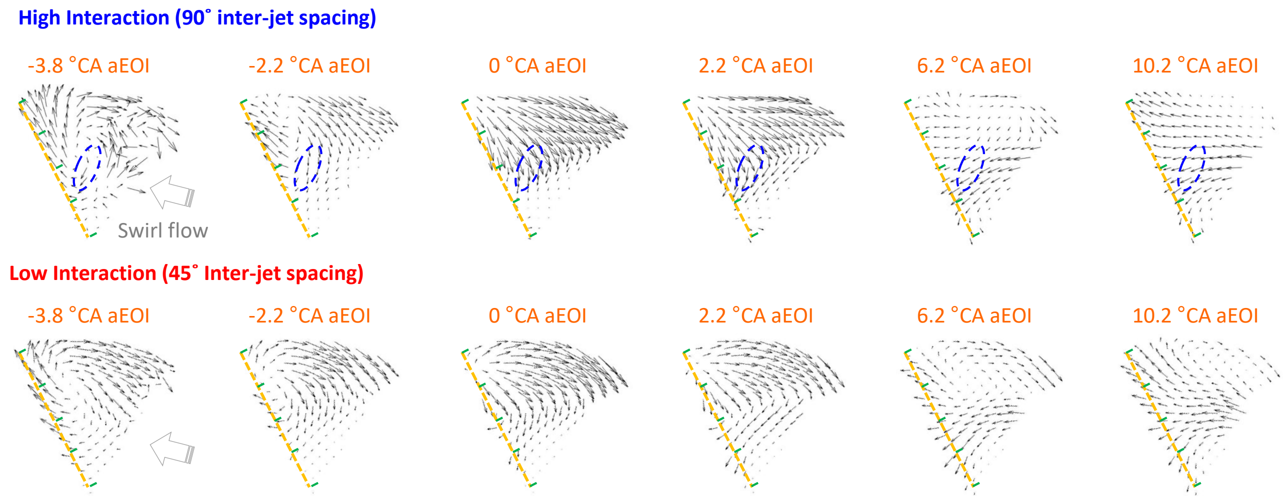

Fig. 10 100-cycle averaged FIV flow fields of high flame-plug interaction and low flame-plug interaction cases during the wall-interaction flame development. The 60° sector is shown for the right side of Jet 2 axis with the glow plug illustrated for the high interaction case. For the low interaction case, the glow plug is outside the region of interest.

3.4 In-flame bulk flow magnitude and turbulence intensity

In Figure 11, the bulk flow magnitude and turbulence intensity within the selected sector regions are plotted for both the high and low interaction cases. Upon the start of combustion, the bulk flow magnitude is measured high during the injection which quickly declines after the end of injection for both cases. The high magnitude region is found near the bowl wall regions within the wall jet heads. The high interaction case displays higher bulk flow magnitude than the low interaction, which remains for a longer distance from the wall to the nozzle in the flame bouncing-off path. This indicates the bouncing-off flow towards the nozzle is stronger as the plug tip blocks the swirl flow to shift its direction. For the measured turbulence intensity, the trend is similar with that observed from the bulk flow magnitude. The turbulence intensity decreases with an increasing crank angle, due to the injection momentum dissipation. High turbulence intensity is found near the bowl wall, while the high interaction case is measured slightly higher than the low interaction condition, especially at the interface of the flame and plug. This suggests the enhanced wall bounced flame and more significant flame-plug interaction leads to enhanced turbulence intensity and thus promoting the mixing.

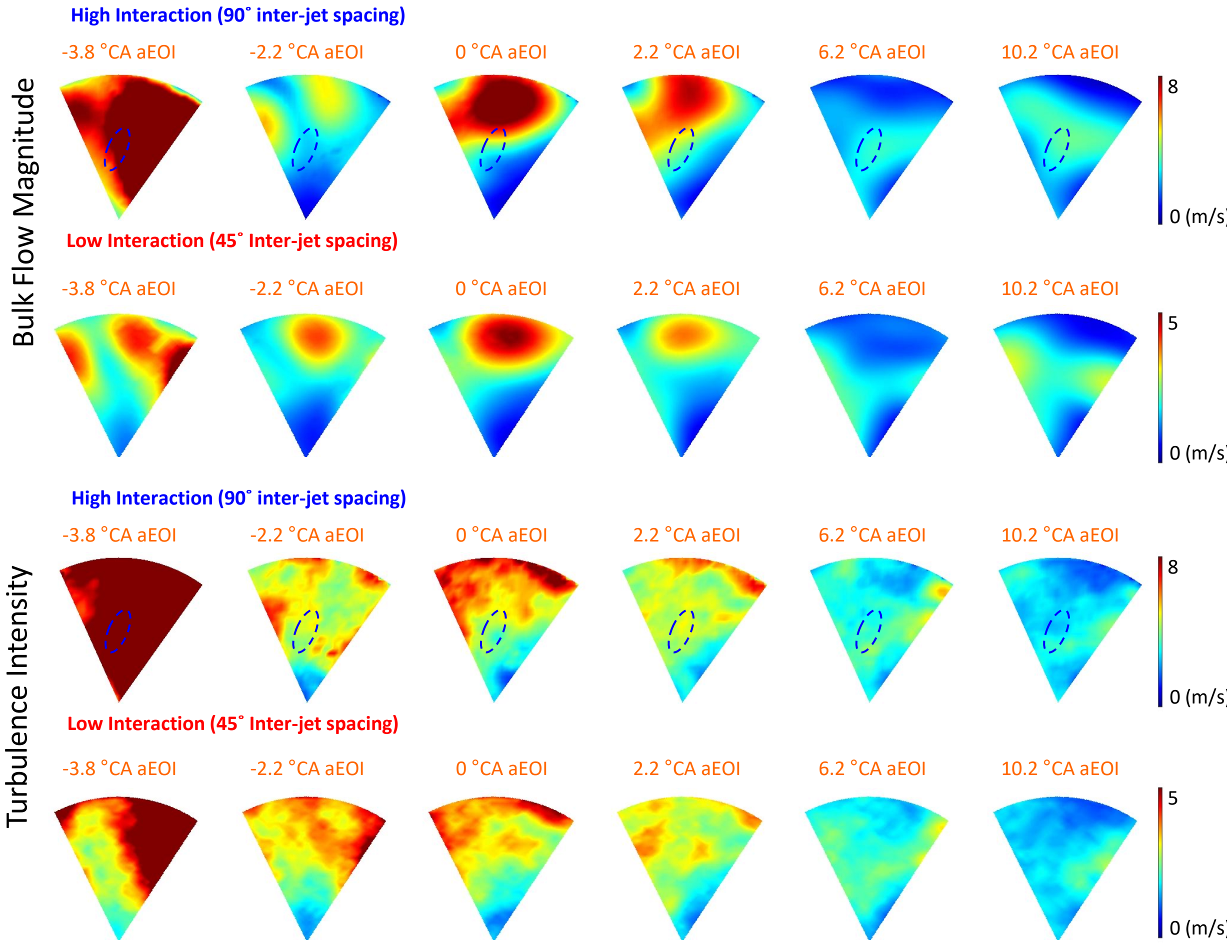

Fig. 11 100-cycle averaged FIV bulk flow magnitude and turbulence intensity distribution of high flame-plug interaction and low flame-plug interaction cases during the wall-interaction flame development.

4. Conclusions

The present study performed two diagnostic methods including PIV and FIV in an optical diesel engine with a particular interested in the glow plug effects on in-cylinder flow and in-flame flow. For each measurement, a total of 100 individual engine cycles were recorded and processed to address the cyclic variations. The PIV derived flow fields showed the flow winding around the plug tip generates a new flow component, leading to increased turbulence intensity downstream the intake flow and plug. However, the increased turbulence is a localised behaviour. During the combustion, two different levels of flame-plug interaction cases were investigated through applying FIV on the flame images. Further penetration of the wall bounced flame was measured for the high interaction case due to stronger flame-plug interaction. The flow fields indicated the glow plug blocks the swirl flow and thus promotes the flame penetration back towards the centre of the combustion chamber. The turbulence intensity is also higher resulting from the enhanced wall bounced flame and more significant flame-plug interaction at the interface.

Acknowledgements

The experiments were performed at the UNSW Engine Research Laboratory, Sydney, Australia. The authors thank to Mr Bryce Edmonds for his technical support and to Dr Dongchan Kim for his scientific inputs. The financial support for this work was provided by DEVCOM Army Research Laboratory and International Technology Center Indo-Pacific (ITC-IPAC).

References

Adrian, R. J., & Westerweel, J. (2011). *Particle image velocimetry* (No. 30). Cambridge university press.

Baum, E., Peterson, B., Böhm, B., & Dreizler, A. (2014). On the validation of LES applied to internal combustion engine flows: part 1: comprehensive experimental database. *Flow, turbulence and combustion*, 92(1), 269-297.

Broday, D. M., & Rosenzweig, R. (2011). Deposition of fractal-like soot aggregates in the human respiratory tract. *Journal of Aerosol Science*, 42(6), 372-386.

Clark, L. G., & Kook, S. (2018). Correlation of spatial and temporal filtering methods for turbulence quantification in spark-ignition direct-injection (SIDI) engine flows. *Flow, Turbulence and Combustion*, 101(1), 161-189.

Clark, L. G., & Kook, S. (2018). Influence of injection timing on large-scale in-cylinder flow in an SIDI engine. In *19th International Symposium on Applications of Laser and Imaging Techniques to Fluid Mechanics, Lisbon, Portugal*.

Cosadia, I., Borée, J., & Dumont, P. (2007). Coupling time-resolved PIV flow-fields and phase-invariant proper orthogonal decomposition for the description of the parameters space in a transparent Diesel engine. *Experiments in fluids*, 43(2), 357-370.

Dembinski, H., & Angstrom, H. E. (2013, April). Swirl and injection pressure impact on after-oxidation in diesel combustion, examined with simultaneous combustion image velocimetry and two colour optical method. In *SAE 2013 World Congress & Exhibition* (No. 2013-01-0913).

Dembinski, H., Ångström, H. E., & Razzaq, H. (2013). In-cylinder flow pattern evaluated with combustion image velocimetry, CIV, and CFD calculations during combustion and post-oxidation in a HD diesel engine. In *SAE 11th International Conference on Engines & Vehicles; Capri, Napoli, Italy, September 15-19, 2013*.

Dembinski, H., & Ångström, H. E. (2013). Swirl and injection pressure effect on post-oxidation flow pattern evaluated with combustion image velocimetry, CIV, and CFD simulation. In *SAE/KSAE 2013 International Powertrains, Fuels & Lubricants Meeting*.

Dembinski, H. W. (2014). The effects of injection pressure and swirl on in-cylinder flow pattern and combustion in a compression–ignition engine. *International Journal of Engine Research*, 15(4), 444-459.

Dembinski, H., & Ångström, H. E. (2012). Optical study of swirl during combustion in a CI engine with different injection pressures and swirl ratios compared with calculations. In *SAE 2012 World Congress, Detroit, USA, April 24-26, 2012*. Society of Automotive Engineers.

Genzale, C. L., Reitz, R. D., & Musculus, M. P. (2009). Effects of spray targeting on mixture development and emissions formation in late-injection low-temperature heavy-duty diesel combustion. *Proceedings of the combustion institute*, 32(2), 2767-2774.

Heim, D., & Ghandhi, J. (2011). A detailed study of in-cylinder flow and turbulence using PIV. *SAE International Journal of Engines*, 4(1), 1642-1668.

Jakobson, L. (2010). China prepares for an ice-free Arctic. *SIPRI insights on peace and security*, 2010(2).

Le Roy, O., & Le Penven, L. (1998). Compression of a turbulent vortex flow. *International journal of heat and fluid flow*, 19(5), 533-540.

Malbec, L. M., & Bruneaux, G. (2010). Study of air entrainment of multi-hole diesel injection by particle image velocimetry-effect of neighboring jets interaction and transient behavior after end of injection. *SAE International Journal of Engines*, 3(1), 107-123.

Miles, P. C., Collin, R., Hildingsson, L., Hultqvist, A., & Andersson, Ö. (2007). Combined measurements of flow structure, partially oxidized fuel, and soot in a high-speed, direct-injection diesel engine. *Proceedings of the combustion institute*, 31(2), 2963-2970.

Neal, N. J., Jordan, J., & Rothamer, D. (2013). Simultaneous measurements of in-cylinder temperature and velocity distribution in a small-bore diesel engine using thermographic phosphors. *SAE International Journal of Engines*, 6(1), 300-318.

Payri, F., Benajes, J., Margot, X., & Gil, A. (2004). CFD modeling of the in-cylinder flow in direct-injection Diesel engines. *Computers & fluids*, 33(8), 995-1021.

Rabault, J., Vernet, J. A., Lindgren, B., & Alfredsson, P. H. (2016). A study using PIV of the intake flow in a diesel engine cylinder. *International Journal of Heat and Fluid Flow*, 62, 56-67.

Reuss, D. L., Kuo, T. W., Khalighi, B., Haworth, D., & Rosalik, M. (1995). Particle image velocimetry measurements in a high-swirl engine used for evaluation of computational fluid dynamics calculations. *SAE transactions*, 2073-2092.

Shioji, M., Kimoto, T., Okamoto, M., & Ikegami, M. (1989). An analysis of diesel flame by picture processing. *Transactions of the Japan Society of Mechanical Engineers Series B*, 54(504), 2228–2235.

Westerweel, J. (1997). Fundamentals of digital particle image velocimetry. *Measurement science and technology*, 8(12), 1379.

Westerweel, J., & Scarano, F. (2005). Universal outlier detection for PIV data. *Experiments in fluids*, 39(6), 1096-1100.

Winterbone, D. E., Yates, D. A., Clough, E., Rao, K. K., Gomes, P., & Sun, J. H. (1994). Combustion in high-speed direct injection diesel engines—a comprehensive study. *Proceedings of the Institution of Mechanical Engineers, Part C: Journal of Mechanical Engineering Science*, 208(4), 223-240.

Yang, J., Rao, L., Zhang, Y., de Silva, C., & Kook, S. (2021). Flame image velocimetry analysis of reacting jet flow fields with a variation of injection pressure in a small-bore diesel engine. *International Journal of Engine Research*, 22(9), 2968-2981.

Zeng, W., Sjöberg, M., & Reuss, D. (2014). Using PIV measurements to determine the role of the in-cylinder flow field for stratified DISI engine combustion. *SAE International Journal of Engines*, 7(2), 615-632.

Zeng, W., Sjöberg, M., & Reuss, D. L. (2015). Combined effects of flow/spray interactions and EGR on combustion variability for a stratified DISI engine. *Proceedings of the Combustion Institute*, 35(3), 2907-2914.

Zha, K., Busch, S., Miles, P. C., Wijeyakulasuriya, S., Mitra, S., & Senecal, P. K. (2015). Characterization of flow asymmetry during the compression stroke using swirl-plane PIV in a light-duty optical diesel engine with the re-entrant piston bowl geometry. *SAE International Journal of Engines,* 8(4), 1837-1855.

Zha, K., Busch, S., Warey, A., Peterson, R. C., & Kurtz, E. (2018). A study of piston geometry effects on late-stage combustion in a light-duty optical diesel engine using combustion image velocimetry. *SAE International Journal of Engines*, 11(6), 783-804.

Zhang, Y., Kim, D., Rao, L., Kook, S., Kim, K. S., & Kweon, C. B. (2019). In-flame soot particle structure on the up-and down-swirl side of a wall-interacting jet in a small-bore diesel engine. *Proceedings of the Combustion Institute*, 37(4), 4847-4855.

Zhao, M., & Kaiser, S. A. (2018). Optical diagnostics for knock in compression-ignition engines via high-speed imaging. *SAE International Journal of Engines*, 11(6), 903-918.